

Title	Simulations of 3D nanoscale architectures and electrolyte characteristics for Li-ion microbatteries
Authors	Clancy, Tomás M.;Rohan, James F.
Publication date	2019-03-07
Original Citation	Clancy, T. M. and Rohan, J. F. (2019) 'Simulations of 3D nanoscale architectures and electrolyte characteristics for Li-ion microbatteries', Journal of Energy Storage, 23, pp. 1-8. doi: 10.1016/j.est.2019.02.002
Type of publication	Article (peer-reviewed)
Link to publisher's version	http://www.sciencedirect.com/science/article/pii/S2352152X18305371 - 10.1016/j.est.2019.02.002
Rights	© 2019 Published by Elsevier Ltd. All rights reserved. This manuscript version is made available under the CC-BY-NC-ND 4.0 license - http://creativecommons.org/licenses/by-nc-nd/4.0/
Download date	2025-04-26 07:01:33
Item downloaded from	https://hdl.handle.net/10468/7587



UCC

University College Cork, Ireland
Coláiste na hOllscoile Corcaigh

Simulations of 3D nanoscale architectures and electrolyte characteristics for Li-ion microbatteries.

Tomás M. Clancy^a and James F. Rohan^{a*}

^a Electrochemical Materials & Energy, Tyndall National Institute, University College Cork, Ireland

*Corresponding author: James Rohan, Tyndall National Institute, University College Cork, Lee Maltings, Cork, Ireland. Tel.: +353 21 234 6224

E-mail address: james.rohan@tyndall.ie

Highlights

- 3D nanoscale electrode architecture geometries have been simulated and compared for microbattery performance.
- The simulations include different electrolyte characteristics for a range of electrode geometries.
- 3D core-shell nanoarchitectures show improved performance for both polymer gel or liquid electrolytes.
- 3D nanoarchitectures with optimised electrolytes can improve battery areal energy and power performance.

Keywords

Finite element simulations

Planar thin-film microbattery

3D nanoarchitectures

Ionic conductivity

Abstract

Finite element simulations are presented, showing material utilisation and electrochemical cell behaviour of a rechargeable Li-ion microbattery in planar thin-film, 3D and 3D core-shell nanoarchitectures in which the active material is 250 nm thick as a shell on a 250 nm diameter core support. The materials simulated are non-porous additive-free LiCoO_2 , lithium metal and solid-state, polymer, polymer-gel and liquid electrolytes. The concentration profile of the LiCoO_2 during discharge and areal energy versus areal power in a Ragone plot for each of the different architectures are compared. It is shown that the planar thin-film architecture gave better cell performance when used with the solid-state electrolyte with all three architectures showing material utilisation of the cathode at the closest point to the anode. The 3D and 3D core-shell nanoarchitectures show better battery performance for the polymer electrolyte than the planar thin film, with the 3D nanoarchitecture being the best. The 3D core-shell architecture shows a significant improvement in performance by comparison with the thin-film and 3D nanoarchitectures when a polymer-gel or a liquid electrolyte are used. The 3D nanoarchitecture shows a slight decline in performance when going from a polymer-gel electrolyte to a liquid electrolyte with faster Li-ion transport. The 3D core-shell nanoarchitecture shows improved cell performance with faster Li-ion transport. The adoption of 3D nanoarchitectures with suitable electrolytes can have a significant improvement in battery areal energy and power performance.

1. Introduction

The internet of things (IoT) scenario is the seamless mass distribution of sensors into everyday objects which enable a smart, efficient and connected world. These sensors are becoming smaller ($<1\text{mm}^3$) and more energy efficient creating a demand for micro energy supplies. Energy harvesters are now able to harvest enough energy from the sensors environment to power these sensors and create an efficient energy cycle[1]. Electrical energy storage technology is needed to enable the commercialisation of energy harvesters as an energy source for IoT sensors due to the intermittency of sources in the environment such as solar or vibrational energy harvesters. A hybrid system would result in a smaller battery capacity requirement and sensors with a lifetime in years rather than months.

However, meeting the energy and power densities (rate at which energy can be accessed) requirements for these devices is proving challenging. Lithium-ion batteries are a mature technology and a leading contender for integration with microelectronic devices for the energy storage provision. Planar thin-film solid-state batteries processed on silicon substrates with excellent cycle life are being developed for such devices but generally suffer from capacity per unit footprint and low power capabilities[2]. This necessitates complex power management circuits and additional components to ensure compatibility, thus drastically increasing the size of the device. Typical thin-film solid-state batteries are made up of an electrolyte that has low lithium ion conductivity. The cathode material is a solid additive-free metal oxide with poor ionic and electronic conductivity which limits the thickness to micrometers ($< 5 \mu\text{m}$) in a 2D geometry, therefore limiting the energy storage per area (Wh cm^{-2}).

Micro and nano-scale fabrication techniques have advanced in recent years and it is now possible to fabricate complex 3D micro and nanoarchitectures[3-5]. 3D architectures can decrease the

distance between anode and cathode while also increasing the surface area of the electrodes. This decrease in distance and increase in surface area means a shorter ion transport distance and improved current distribution which results in higher power densities. A range of complex 3D architectures have been proposed as suitable geometries for lithium-ion batteries with high energy and power densities[6]. Depending on the critical material characteristics of the anode, cathode and electrolyte the 3D architectures may actually have a deleterious effect on cell performance if not optimised.

Mathematical modelling is used to describe the underlying electrochemical characteristics to optimise the 3D architecture. Finite element analysis (FEA) is a powerful tool for optimisation of battery design, highlighting the key material and operational parameters to tailor the battery architecture for various applications. Examples of where FEA has been used to simulate micron scale battery materials and architectures include the work of Hart et al. optimising the electrode array configuration in a 3D microbattery which highlighted the significant impact that non-uniform primary current distribution has on the battery performance[7]. Zadin et al. provided simulations of 3D micron scale architectures such as concentric pillars, interdigitated trenches and pillars using both non-porous and porous electrode electrochemistry models[8-11]. Miranda et al. investigated the effect of different geometries from conventional layered geometries to unconventional geometries such as antenna and gear shaped electrodes[12]. They also assessed how the battery performance could be tailored for certain applications by modifying the micron scale dimensions.

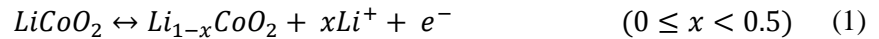
FEA of Li-ion batteries are generally built on the foundation of the work carried out by Newman and co-workers who developed the isothermal electrochemical model[13]. The charge and transport of battery species are dictated by the concentration gradient of lithium ions and the electrochemical potential gradient. There are a number of phases in the battery, anode, cathode

and electrolyte, which need to be considered when implementing the conversion principles and equations to describe the transport of species and charge. The mass transport in the electrolyte, potential difference and profile in the anode and cathode materials are critical in predicting the battery performance. Newman et al. highlighted the significant effect that electrode porosity has on cell performance[14]. FEA simulations using COMSOL have been presented by Danilov et al. for all solid-state Li-ion batteries[15]. The aim of this paper is to compare the electrochemical performance of planar thin-film microbatteries to 3D nanoscale architecture Li-ion battery materials for solid-state, polymer, polymer-gel and liquid electrolytes.

2. Materials and methods

2.1 Theoretical Considerations

Conventional Li-ion battery materials characteristics were used in this study. The anode electrode is metallic lithium, cathode electrode is LiCoO₂. The electrode materials are considered to be non-porous and additive free. This means that Li-ion transport can only be considered at the electrolyte/electrode interface. The electrolytes used can be grouped into solid-state, polymer, polymer-gel and liquid electrolytes. The solid-state electrolyte material is based on an amorphous LIPON, derived from Li₃PO₄ sputter targets in a nitrogen environment and the polymer, polymer-gel and liquid electrolyte material based on 1M LiPF₆ salt dissolved polymer and solvent. The electrochemical reaction that takes place at each electrode is:



Li-ion concentration in LiCoO₂ is at its maximum when the battery is fully discharged and at its lowest when the battery is fully charged.

2.2 Mathematical model

Multiphysics simulations were computed using COMSOL Multiphysics® Version 5.0 software. The lithium-ion battery and transport of diluted species modules have predefined mathematical equations which were used to describe mass transport in the electrolyte and electrode respectively. In this work a combination of the Doyle et al. and Danilov et al models describe the main equations that dictate the operation of a battery[13, 15]. The following assumptions are made for this mathematical model:

1. Diffusion coefficients and conductivities are constant for the materials in the respective regions studied. For the nanoscale materials studied the differences with the extent of lithiation are significantly less than the orders of magnitude differences in conductivity and diffusion on changing the electrolyte system or the use of a core metallic electronic conductor rather than the poorly conducting oxide material.
2. Ion movement in the solid non-porous electrodes is described by diffusion.
3. No side reactions are considered.
4. The electrolyte is in electroneutrality at all times.
5. No volume changes occur in the electrodes.
6. At the electrolyte/electrode interface the charge transfer processes are described using Butler-Volmer kinetics:

$$J = i_0 \left[\exp\left(F\alpha_a \frac{\eta}{RT}\right) - \exp\left(-F\alpha_c \frac{\eta}{RT}\right) \right] \quad (3)$$

where J is the current density at the electrolyte/electrode interface, i_0 is the exchange current density and α_a and α_c are the anodic and cathodic transfer coefficients where $\alpha_c = 1 - \alpha_a$.

7. The transference number (t_0) and the activity coefficient $\left(\frac{\partial \ln f}{\partial \ln(c_{Li_{ion}})}\right)$ throughout the electrolyte are constant.

The surface overpotential, η , at the interface is:

$$\eta = \varphi_{Li} - \varphi_{Li_{ion}} - U_{oc} \quad (4)$$

where φ_{Li} and $\varphi_{Li_{ion}}$ are the potentials of the electrode and electrolyte respectively and U_{oc} is the open circuit potential function. The experimental open circuit potential of the electrodes is fitted to a polynomial function. The equilibrium and electric potential for lithium metal anode electrode is set to 0. The equilibrium potential for LiCoO₂ cathode electrode is dependent upon its ion concentration.

The exchange current density is described by:

$$i_0 = Fk(c_{-Li}c_{Li_{ion}})^{\alpha_a}(c_{Li})^{\alpha_c} \quad (5)$$

where k is the Butler-Volmer reaction rate coefficient, c_{-Li} is the remaining available ion concentration in the electrode, $c_{Li_{ion}}$ is the dissociated ion concentration in the electrolyte and c_{Li} is the ion concentration in the electrode. c_{-Li} can be rewritten as $c_{-Li} = (c_{Li_{max}} - c_{Li})$ where $c_{Li_{max}}$ is the maximum ion concentration in the electrode. The exchange current density, Eq. 5, for the cathode electrode can be rewritten as:

$$i_{0_{pos}} = Fk_{pos} \left[\left(\frac{c_{Li_{max}} - c_{Li}}{c_{Li_{max}} - c_{Li_{min}}} \right) \left(\frac{c_{Li_{ion}}}{c_{0_{Li_{ion}}_{init}}} \right) \right]^{\alpha_{a_{pos}}} \left(\frac{c_{Li} - c_{Li_{min}}}{c_{Li_{max}} - c_{Li_{min}}} \right)^{\alpha_{c_{pos}}} \quad (6)$$

where c_{Li_min} is the minimum ion concentration in the electrode and $c_{0_Li_ion_init}$ is the total ion concentration in the electrolyte. The exchange current density for anode electrode can be simplified since the anode material is lithium metal:

$$i_{0_neg} = Fk_{neg} \left(\frac{c_{Li_ion}}{c_{Li_ion_init}} \right)^{\alpha_{a_neg}} \quad (7)$$

where both c_{-Li} and c_{Li} become negligible as the activity of lithium metal is considered unity.

The potential of the electrodes (φ_{Li}) is calculated using Ohm's law and since the anode material is lithium metal only the cathode is considered.

$$\nabla \cdot (\sigma_{Li_pos} \nabla \varphi_{Li}) = 0 \quad (8)$$

$$\vec{n} \cdot (\sigma_{Li_pos} \nabla \varphi_{Li}) = J \quad (9)$$

The potential of the electrolyte (φ_{Li_ion}) is calculated using Ohm's law and the concentrated solution theory:

$$\nabla \cdot (\sigma_{Li_ion} \nabla \varphi_{Li_ion} - \sigma_{diff} \nabla \ln(c_{Li_ion})) = 0 \quad (10)$$

$$\vec{n} \cdot (\sigma_{Li_ion} \nabla \varphi_{Li_ion} - \sigma_{diff} \nabla \ln(c_{Li_ion})) = -J \quad (11)$$

where σ_{Li_ion} , σ_{diff} and \vec{n} are the electrolyte ionic conductivity, diffusional conductivity and the normal unit vector respectively. The diffusional conductivity is calculated from:

$$\sigma_{diff} = \frac{2RT\sigma_{Li_ion}}{F} (1 - t_0) \left(1 + \frac{\partial \ln f}{\partial \ln(c_{Li_ion})} \right) \quad (12)$$

as the activity coefficient is assumed constant when the partial term in Eq. 12 is removed.

The transport of lithium through the cathode electrode is calculated using the concentrated solution theory i.e. Fick's law:

$$\frac{\partial c}{\partial t} = \nabla(D_{Li_pos} \nabla c_{Li}) \quad (13)$$

$$\vec{n} \cdot \nabla c_{Li} = \frac{J}{FD_{Li_pos}} \quad (14)$$

where D_{Li_pos} is the diffusion coefficient of lithium in the cathode electrode and Eq. 14 describes the boundary condition at the electrolyte/electrode interface.

Typical lithium conducting solid-state electrolytes are glass-like. This glass-forming system operates in which the lithium ions are transported in a shuttle type movement, where the bridging oxygen atoms in a quasi-two-dimensional polymeric network are depolymerized in the presence of a modifier to non-bridging oxygen atoms. The ionized reaction, Eq. 15, therefore is the transformation of immobile oxygen-bound lithium (Li^0) to mobile lithium (Li^+) with resultant negative charge (n^-) chemically associated to the nearest non-bridging oxygen atom.



k_d is the dissociation rate coefficient of Li^0 and k_r is the recombination rate coefficient of ($Li^+ + n^-$). The overall rate of the dissociation reaction is:

$$r_{Li_ion} = k_d(c_{0_Li_ion_init} - c_{Li_ion}) - k_r(c_{Li^+})(c_{n^-}) \quad (16)$$

When the solid-state electrolyte is at equilibrium the fraction of Li^+ in $c_{0_Li_ion_init}$ is δ . Since the electrolyte is assumed to be electroneutral the equilibrium of the mobile charge carriers and immobile lithium is:

$$c_{Li^+}^{Eq} = c_{n^-}^{Eq} = \delta c_{0_Li_ion_init} \quad (17)$$

$$c_{Li^0}^{Eq} = (1 - \delta)c_{0_Li_ion_init} \quad (18)$$

$$k_d c_{Li^0}^{Eq} = k_r c_{Li^+}^{Eq} c_{n^-}^{Eq} \quad (19)$$

Combining Eqs. 17, 18, 19 gives the dissociation rate of reaction in the solid-state electrolyte:

$$k_d = \frac{k_r c_{0_Li_ion_init} \delta^2}{(1 - \delta)} \quad (20)$$

The transport of lithium through the solid-state electrolyte is calculated using the concentrated solution theory and the electrolyte rate coefficient:

$$\frac{\partial c}{\partial t} = \nabla(D_{Li_ion} \nabla c_{Li_ion}) + r_{Li_ion} \quad (21)$$

The rate coefficient is not utilised when a liquid electrolyte is used as it is assumed to be fully dissociated. The boundary condition at the electrolyte/electrode interface, anion diffusion, has to be taken into account and is balanced by migration $(1 - t_0)$.

The general and electrolyte parameters utilised are listed in tables 1 and 2, respectively.

$$\vec{n} \cdot \nabla c_{Li_ion} = \frac{J(1 - t_0)}{FD_{Li_ion}} \quad (22)$$

Table 1: COMSOL multiphysics general parameters

Symbol	Description	Value	Reference
c_{Li_max}	Maximum Li concentration in cathode	50.88 mol dm ⁻³	[16]
k_{pos}	Butler-Volmer cathode reaction rate coefficient	5.1x10 ⁻⁴ mol m ⁻² s ⁻¹	[17]
k_{neg}	Butler-Volmer anode reaction rate coefficient	1x10 ⁻² mol m ⁻² s ⁻¹	[17]
σ_{Li_pos}	Cathode electrical conductivity	1x10 ⁻⁵ S cm ⁻¹	[18]
D_{Li_pos}	Cathode diffusion Coefficient	2.93x10 ⁻¹⁰ cm ² s ⁻¹	[19]
σ_{Li_neg}	Anode electrical conductivity	1.05x10 ⁵ S cm ⁻¹	[20]
α_{a_pos}	Cathode transfer coefficient	0.6	[15]
α_{a_neg}	Anode transfer coefficient	0.5	[17]
t_0	Transference number	0.5	[8]
T	Temperature	298.15K	

Table 2: Electrolyte Parameters

Symbol	Description	Value	Reference
$c_{0_Li_ion_init}$	Total concentration of Li-ions in solid electrolyte	60100 mol m ⁻³	[15]
k_r	Li-ion recombination reaction rate in solid electrolyte	0.9x10 ⁻⁸ m ³ mol ⁻¹ s ⁻¹	[15]
δ	Fraction of free Li-ions in equilibrium solid electrolyte	0.18	[15]
	Concentration of dissociated Li-ions in solid electrolyte	$\delta^* c_{0_Li_ion_init}$	[15]
$c_{Li_ion_init}$	Concentration of dissociated Li-ions in liquid electrolyte	1000 mol m ⁻³	[21]
	Diffusion coefficient in solid electrolyte	1x10 ⁻¹¹ cm ² s ⁻¹	[22]
D_{Li_ion}	Diffusion coefficient in polymer electrolyte	1x10 ⁻⁹ cm ² s ⁻¹	[23]
	Diffusion coefficient in polymer-gel electrolyte	1x10 ⁻⁸ cm ² s ⁻¹	[23]
	Diffusion coefficient in liquid electrolyte	1x10 ⁻⁷ cm ² s ⁻¹	[21]
σ_{Li_ion}	Ionic conductivity of solid electrolyte	1x10 ⁻⁶ S cm ⁻¹	[22]
	Ionic conductivity of polymer electrolyte	1x10 ⁻⁵ S cm ⁻¹	[23]

Ionic conductivity of polymer-gel electrolyte	$1 \times 10^{-4} \text{ S cm}^{-1}$	[23]
Ionic conductivity of liquid electrolyte	$1 \times 10^{-3} \text{ S cm}^{-1}$	[21]

2.3 Geometric models

The geometric models used in these studies are the planar thin-film microbattery, 3D and 3D core-shell nanoarchitectures; see Fig. 1. The thin-film microbattery geometry comprised of 2.5 μm thick electrodes separated by 1.25 μm of electrolyte, the width of the microbattery is just a fraction of a typical planar thin-film but matched the same quantity of electrode material as the 3D and 3D core-shell nanoarchitectures.

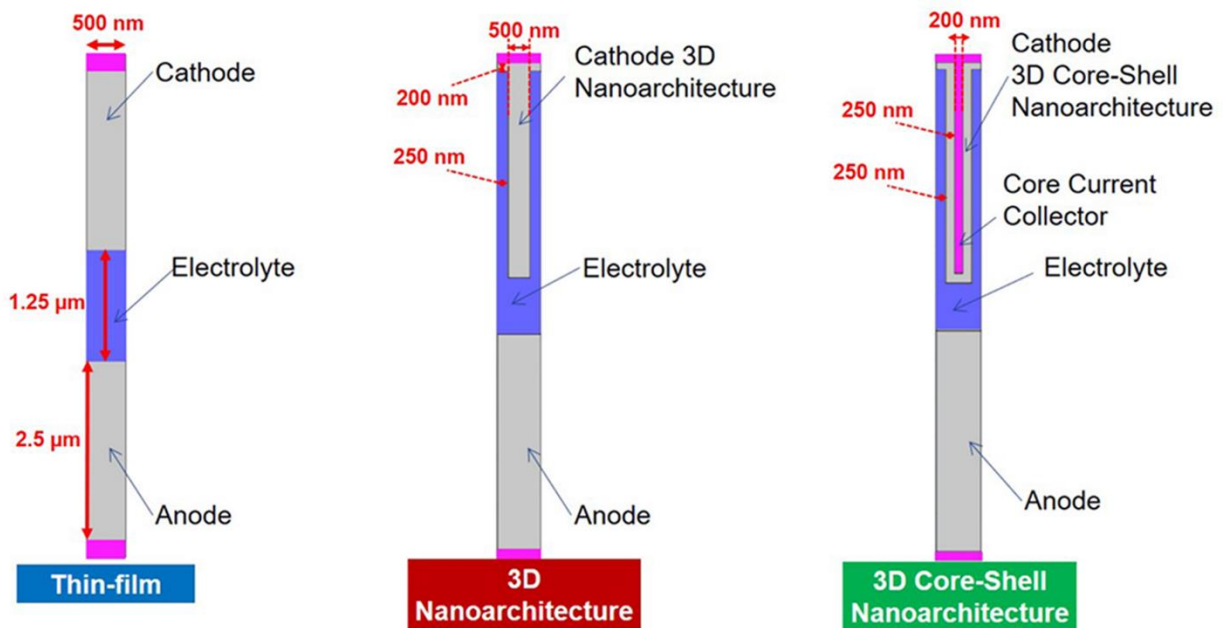


Figure 1: Types of architectures; Thin-film, 3D and 3D core-shell nanoarchitectures.

The 3D nanoarchitecture battery geometry is composed of anode and cathode materials in 3D electrodes with a width of 500 nm, the tops of the electrodes are separated by 1.25 μm and have a spacing of 250 nm filled with electrolyte. The 3D core-shell nanoarchitecture geometry is comprised of a 3D current collector uniformly covered in anode and cathode material. The 3D current collector has a width of 200 nm, covered in 250 nm thick electrode material and a 250 nm spacing filled with electrolyte. The 2D model used in these simulations used an out-of-plane

thickness of 100 μm . The stated battery capacity is based on a full discharge in 7200 seconds equivalent to a 0.5 C rate. The anode and cathode are directly opposite each other for all of the 3 geometries, this is of particular importance for the 3D and 3D core-shell nanoarchitectures for practical fabrication. For solid-state batteries, areal capacity (capacity per overall cell area) is the most important characteristic since area is at a premium; therefore it is important to compare not just the gravimetric energy density but also the areal capacity of the geometries.

For this study an extremely fine edge mesh was used on the electrode/electrolyte boundaries while the mesh for the remaining geometry was extra fine free triangular mesh. A parametric sweep was used to vary the discharge C-rate. The time dependent study was between 0 and 7200 seconds with a relative tolerance of 10^{-4} and a stop condition of a time step $<1 \times 10^{-7}$ s.

3. Results and discussion

To compare a thin-film microbattery with the 3D and 3D core-shell nanoarchitectures on a practical level, the areal capacity at a 0.5 C-Rate of the 3D and 3D core-shell nanoarchitectures must match the areal capacity of the thin-film microbattery. The geometries of the 3D and 3D core-shell nanoarchitectures both require an increase in area to allow for the electrolyte to make contact in and around the base of the nanoarchitectures. The 3D core-shell nanoarchitecture requires an additional increase in area by comparison with the 3D nanoarchitecture to take into account the area of the core current collector, Table 3. Increasing the amount of active electrode material offsets this increase in area. Since the area is fixed the additional active electrode material is accounted for by increasing in the electrode height as seen in Fig. 2.

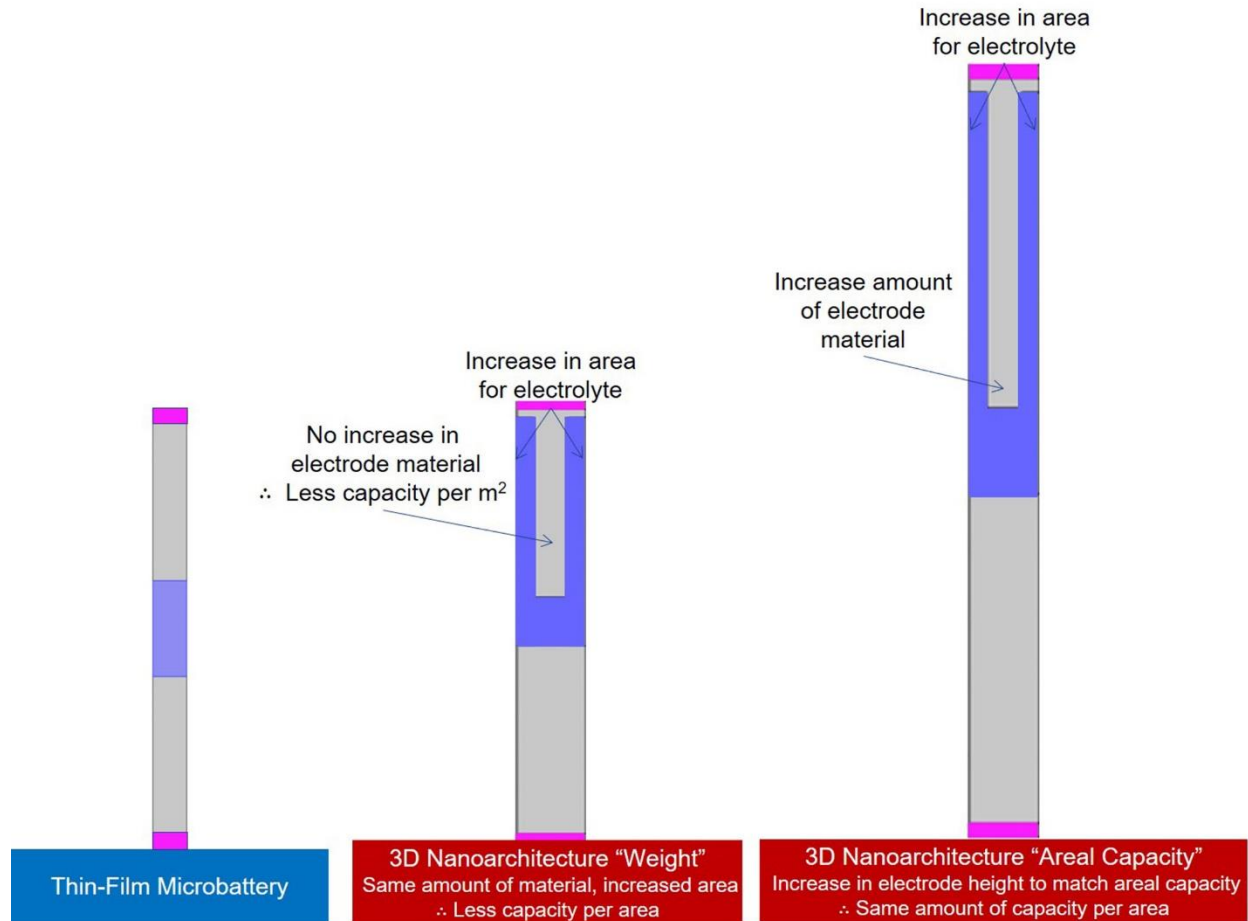


Figure 2: The effect on geometry of a 3D nanoarchitecture to match the areal capacity of planar thin-film microbattery

Table 3: Architecture versus discharge current

Architecture	Cell Width / nm	Discharge Current (1 C) / nA	Current Density / A m ⁻²
Thin-Film	500	0.08441	1.69×10^{-4}
3D Nanoarchitecture	1000	0.16882	1.69×10^{-4}
3D Core-Shell Nanoarchitecture	1200	0.20260	1.69×10^{-4}

The geometric effects on the overall capacity of the battery is dependent on the electrolyte used. As seen in the Ragone plot in Fig. 3 the thin-film microbattery geometry gives superior areal power values in comparison to the 3D and 3D core-shell nanoarchitecture when a solid-state electrolyte is used. This is due to low values of ionic conductivity and diffusion coefficient for the solid-state

electrolyte. The low values for these critical parameters mean that it is faster for the Li^+ ions to diffuse through the cathode material rather than the electrolyte. This negates any advantages associated with the nanoarchitectures such as the electrolyte contact with a larger electrode surface area. In Fig. 4 the advantages of additional surface area in contact with the electrolyte are seen for 3D and 3D core-shell nanoarchitectures when polymer electrolyte characteristics are used.

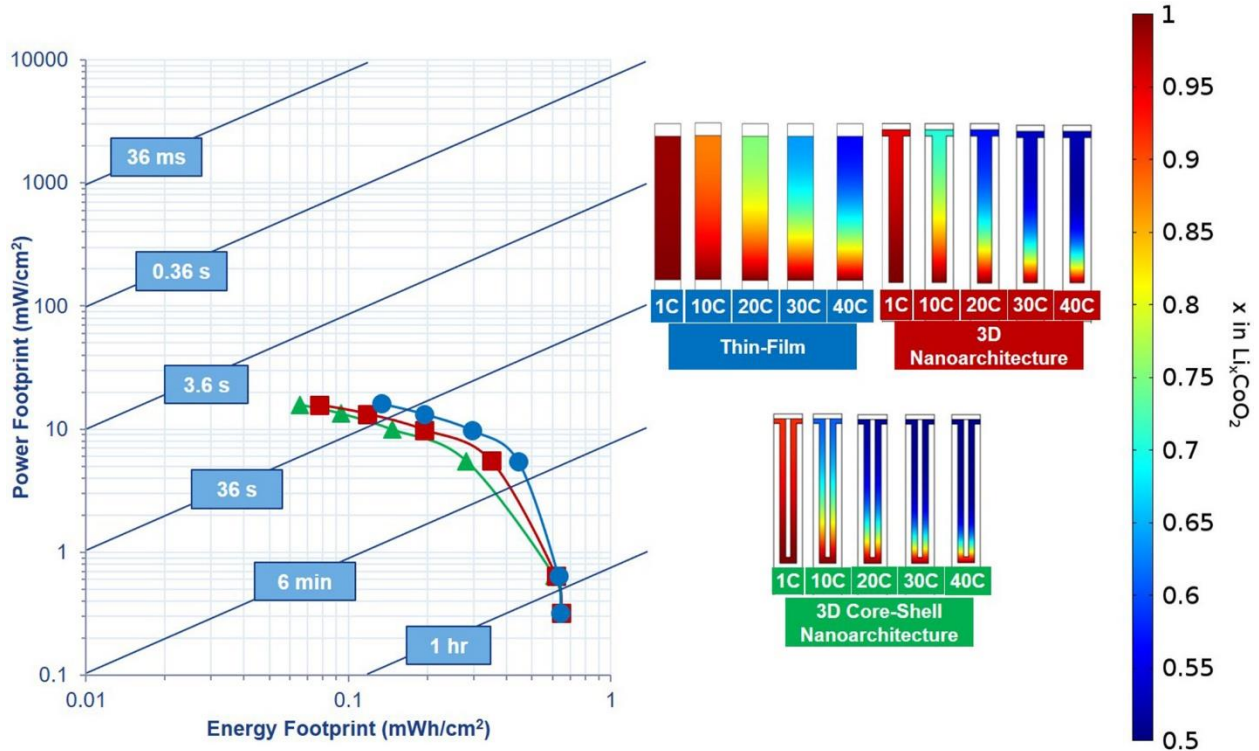


Figure 3: Ragone plot and lithium concentration profile at discharge termination for the C rate indicated of thin-film, 3D and 3D core-shell nanoarchitectures with a solid-state electrolyte.

The 3D nanoarchitecture shows the best power performance in comparison to thin-film microbattery and the 3D core-shell nanoarchitecture. Even though both the 3D and 3D core-shell nanoarchitectures have additional surface area exposed, the core current collector has a negative effect. The additional area for the core current collector comes at a cost resulting in taller electrodes which leads to less uniform lithiation than the 3D nanoarchitecture even at lower C-rates resulting in lower areal power capabilities.

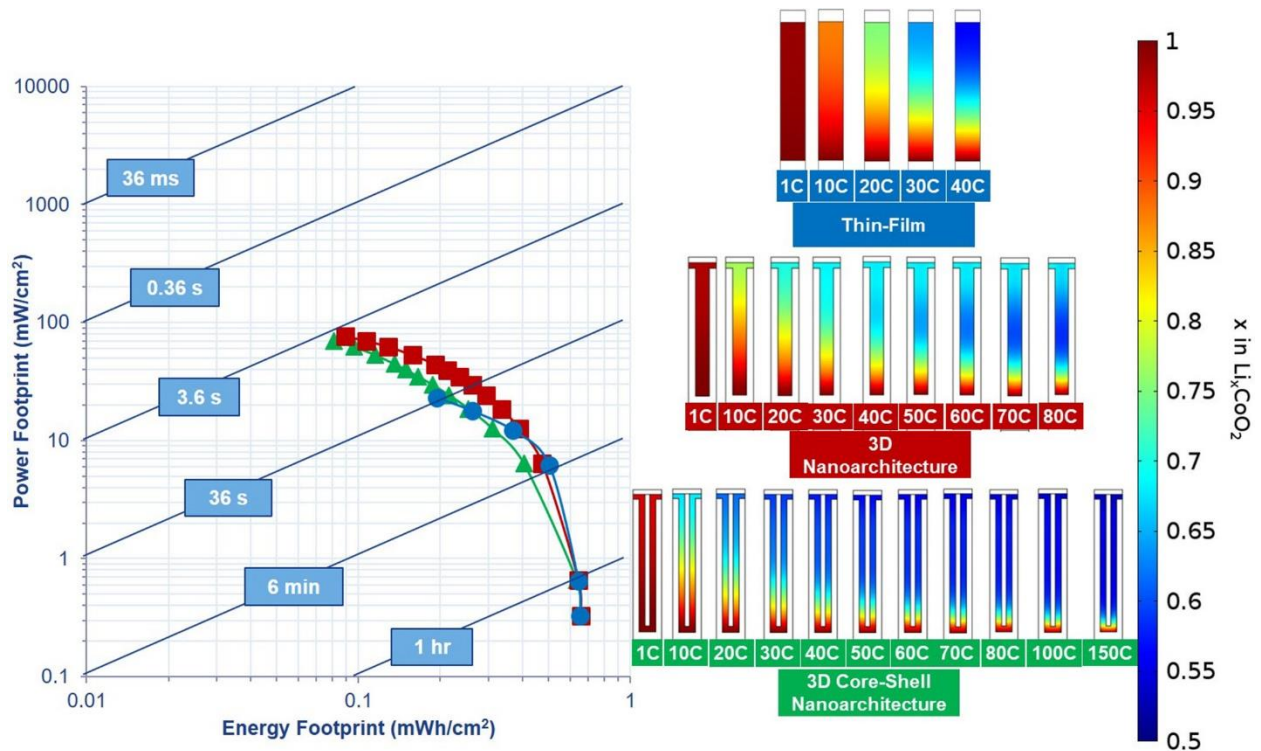


Figure 4: Ragone plot and lithium concentration profile at discharge termination for the C rate indicated of thin-film, 3D and 3D core-shell nanoarchitecture with a polymer electrolyte.

The concentration profile of the 3D nanoarchitecture with a polymer electrolyte shows that at higher C-rates an increased amount of non-utilised electrode material exists at the centre of the 3D nanoarchitecture by comparison with the base and tip of the 3D nanoarchitecture. This is because the transport rate of the Li^+ ions through the electrolyte and the electrode, in this case, are similar. The electrolyte allows for the transport of the Li^+ ions to the base of the electrode closest to the current collector while the diffusion of Li^+ ions through the electrode material is also favourable. The Ragone plot for the polymer-gel electrolyte is shown in Fig. 5 with a larger improvement in the areal power and energy values for the nanoarchitectures by comparison with the polymer electrolyte. The benefit of the core current collector can be seen in this plot and the advantages that the 3D core-shell nanoarchitectures specifically has over the 3D nanoarchitecture without a core. The core current collector improves the electronic transport as the distance between the

electrode/electrolyte interface and the core current collector is much smaller by comparison with the 3D nanoarchitecture format in which the current collector contact is only at the base.

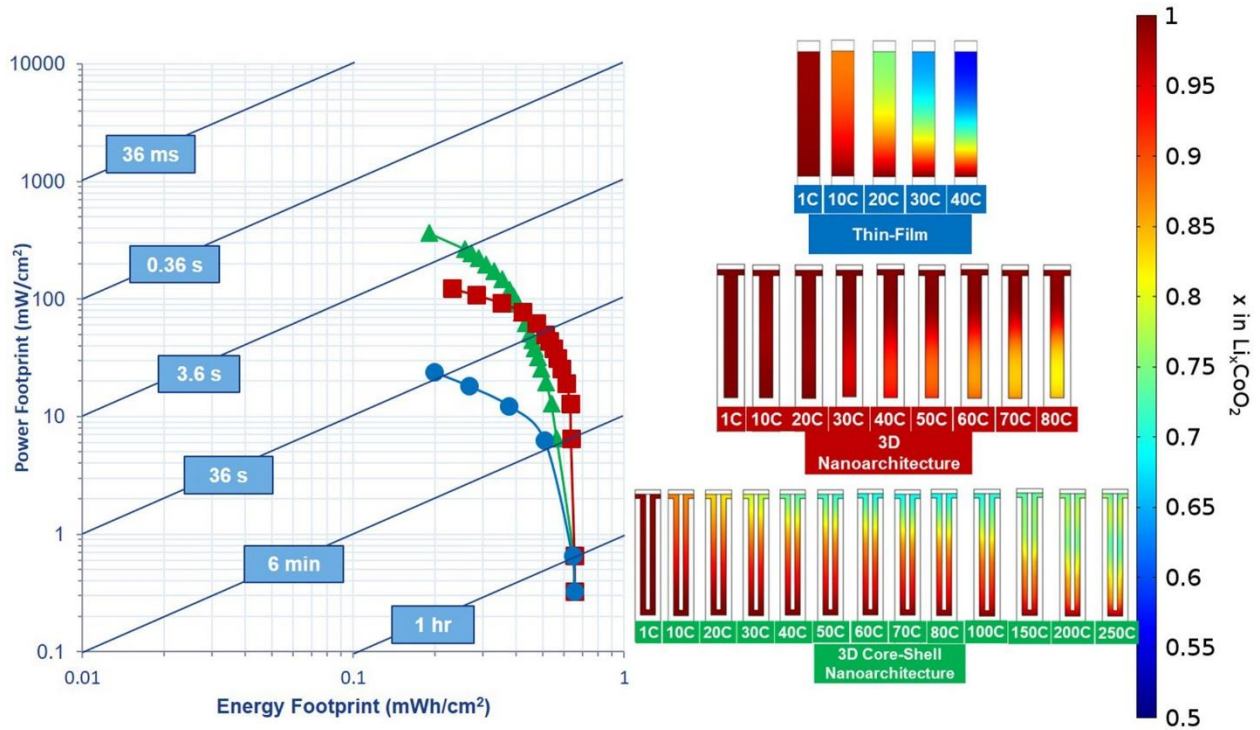


Figure 5: Ragone plot and lithium concentration profile at discharge termination for the C rate indicated of thin-film, 3D and 3D core-shell nanoarchitectures with a polymer-gel electrolyte.

This results in an improved lithiation distribution and a more gradual decline in performance at higher C-rates for the 3D core-shell nanoarchitecture. The improved characteristics of the polymer-gel electrolyte result in very good power and energy values for the 3D nanoarchitecture however these values diminish rapidly at increased C-rates by comparison with the 3D core-shell nanoarchitecture due to the absence of the core current collector.

Liquid electrolyte characteristics for the 3 geometries can be seen in Fig. 6. The positive attributes of the 3D core-shell nanoarchitecture are more prominent in this case and have a significant effect on the areal power and energy values. The liquid electrolyte makes the lithiation process more favourable assisting the Li^+ ions to diffuse through the electrolyte and uniformly around the

electrode due to the core current collector followed by solid-state diffusion into the electrode material.

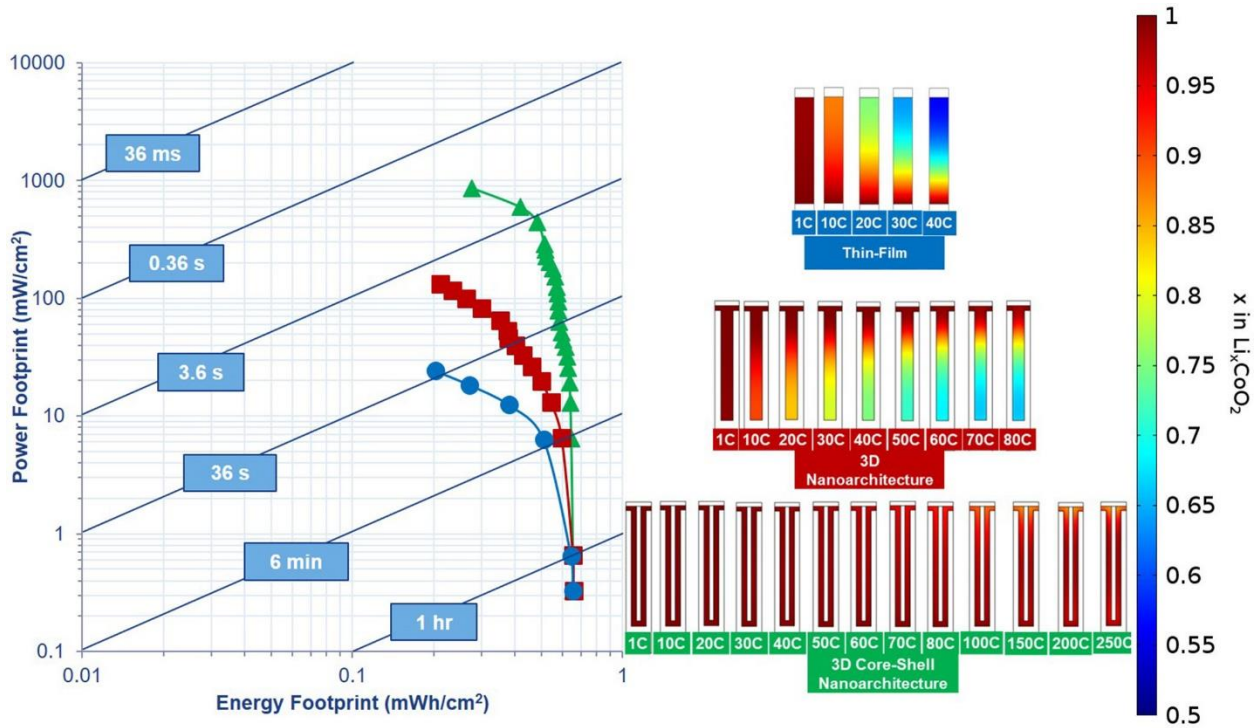


Figure 6: Ragone plot and lithium concentration profile at discharge termination for the C rate indicated of thin-film, 3D and 3D core-shell nanoarchitectures with a liquid electrolyte.

At the higher rates a difference in concentration profiles and the Ragone plots is seen due to the uniformity of lithiation in the electrode. When lithiation is not uniform various local reaction rates occur at the electrode. Areas with a higher reaction rate become fully lithiated faster than the lithium in these areas can diffuse to areas of lower concentration in the electrode. The charging process stops prematurely and not all of the material is accessed at the increased C-rates.

Fig. 7 shows that 3D nanoarchitecture becomes the performance limiting factor and electrolyte characteristics have little or no effect on the cell performance and there is little difference between a 3D nanoarchitecture, used with a polymer-gel or a liquid electrolyte. Both the polymer-gel and liquid electrolyte favour lithium transport through the electrolyte initially and lithiation at the

closest point to the current collector which is at the base of the electrode. Interestingly, the polymer-gel electrolyte shows better performance at lower C-rates up to 80 C due to the coupling of lithium transport mechanisms through the electrolyte to the base of the 3D nanoarchitecture and through the minimum amount of electrolyte to the electrode tip where high rates of lithiation occur

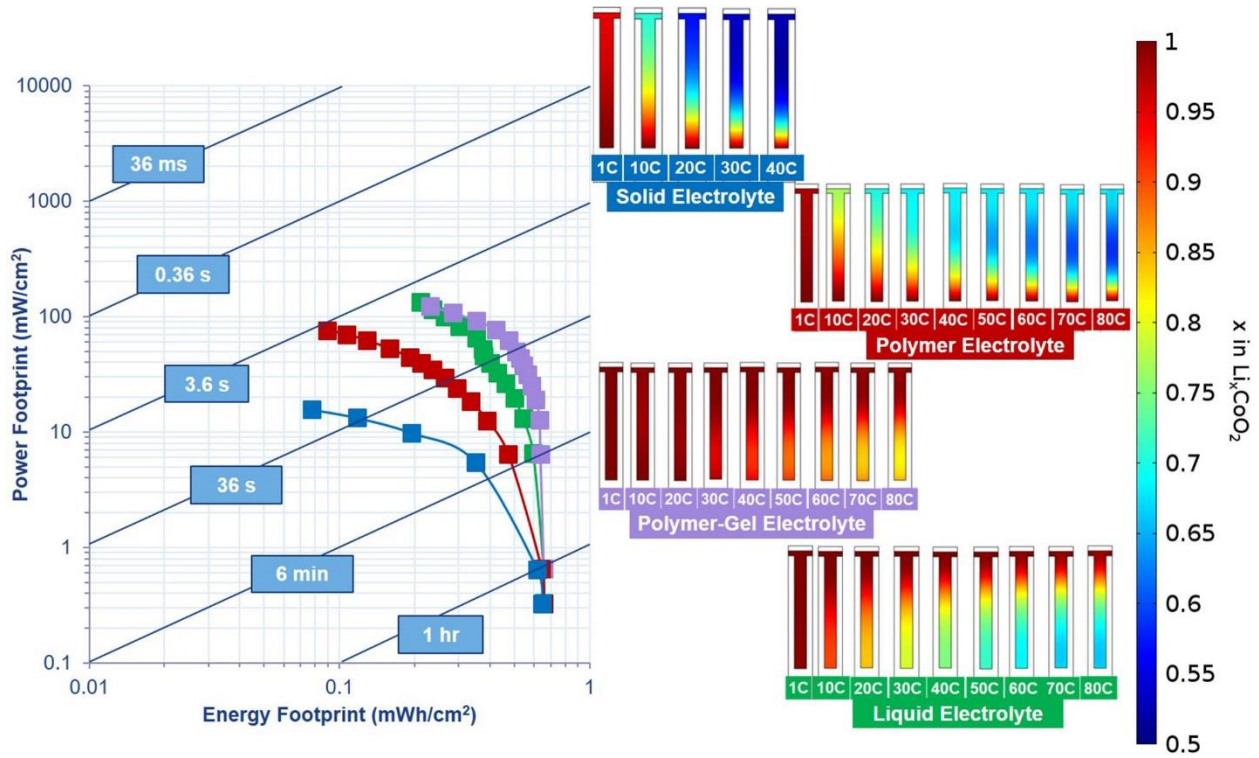


Figure 7: Ragone plot and lithium concentration profile at discharge termination for the C rate indicated of 3D nanoarchitecture with a solid, polymer, polymer-gel and liquid electrolyte.

at both locations. This coupling of lithium transport mechanisms allows for more utilisation of electrode material at lower C-rates, however the slightly less favourable transport mechanism of lithium transport to the tip of 3D nanoarchitecture begins to diminish at increasing C-rates leaving just the lithium transport to the base of the electrode. The slightly slower transport of lithium in the polymer-gel electrolyte compared to the liquid electrolyte means there is a more significant drop off in performance at higher C-rates for the polymer-gel electrolyte. The opposite effect can be seen for the polymer electrolyte where the lithium transport to the base of the 3D

nanoarchitecture is the least favourable transport mechanism and becomes negligible at higher C-rates.

Since the critical kinetic parameters of the polymer electrolyte are lower than the polymer-gel the coupling effect of the lithium transport mechanism is more extreme for the concentration profile at higher C-rates. The liquid electrolyte shows a slightly negative effect at lower C-rates by comparison with the polymer-gel electrolyte solely due to the electrode geometry.

The 3D core-shell nanoarchitecture benefits most from enhanced electrolyte characteristics as seen in Fig. 8. There is a significant increase in cell performance with improving electrolyte characteristics, which is due to the 3D core-shell nanoarchitecture providing more uniform lithiation especially when lithium diffusion in the electrolyte rather than the electrode is the limiting factor. The core current collector minimises the diffusion distance from electrolyte/electrode interface to current collector and has an equal distance from the side wall. When the solid electrolyte is used for the 3D core-shell nanoarchitecture the lithium diffusion through the electrode is faster than through the electrolyte. This causes high local overpotentials at the tip of the 3D core-shell nanoarchitecture which ultimately ends the lithiation process early at increasing C-rates. A similar and delayed response is seen for the polymer electrolyte due to the better electrolyte characteristics. The polymer-gel electrolyte shows a different response. At the 250 C rate it can be seen that there is a slightly higher concentration of lithium near the base than the centre, this is more than likely due to the larger electrode/current collector interface area at the base. A similar but more extreme result can also be seen for the 3D nanoarchitecture. The liquid electrolyte shows uniform lithiation throughout the electrode at high C-rates.

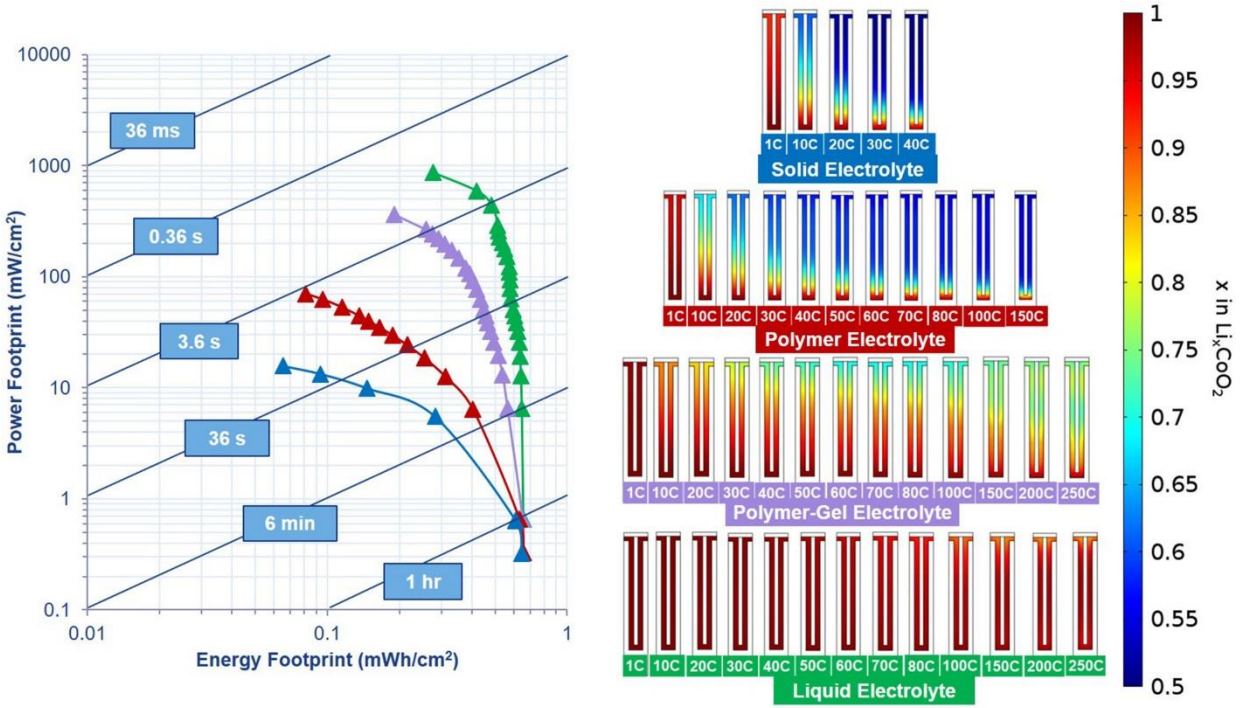


Figure 8: Ragone plot and lithium concentration profile at discharge termination for the C rate indicated of 3D core-shell nanoarchitecture with a solid, polymer, polymer-gel and liquid electrolyte.

The liquid electrolyte coupled with the 3D core-shell nanoarchitecture gave the best performance, for a 1500 C (2.4 s) discharge rate, in which 42% (0.28 mWh cm⁻²) of the battery is utilised with an areal power value of 862 mW cm⁻². This is a dramatic improvement from the thin-film battery with the solid-state electrolyte where a 20 C (180 s) discharge rate gave 47% (0.30 mWh cm⁻²) of the batteries areal energy with an areal power of 9.71 mW cm⁻². Even if the electrolyte is changed to a liquid electrolyte only a slight improvement is seen in the battery cell performance, 30 C (120 s) discharge gave 42% (0.27 mWh cm⁻²) of the total areal energy with an areal power of 18.35 mW cm⁻².

4. Conclusions

In this work, FEA has been used to compare the effect of different architectures on a range of electrolytes and the influence of the different electrolytes on the optimised nanoscale active

material and architecture. The simulations were of a microbattery stack where non-porous additive-free LiCoO_2 is the cathode, lithium metal is the anode and solid-state, polymer, polymer-gel and liquid electrolytes were investigated. The architectures used are planar thin film, 3D and 3D core-shell nanoarchitectures where the anode and cathode are directly opposite each other for nanoarchitecture fabrication practicality. The simulations include Fick's diffusion law for lithium transport in the electrode, concentration solution theory for the transport of Li^+ ions in the electrolyte and the Butler-Volmer theory to describe the transport kinetics at the electrode/electrolyte interface.

When comparing the effect the geometries have on the solid-state electrolyte it can be concluded that thin-film microbatteries have slightly better performance by comparison with 3D and 3D core shell nanoarchitectures. This is because the electrodes height needs to be increased to accommodate for the additional footprint of a 3D (electrolyte in contact with electrode sidewall) and 3D core-shell (addition on core current collector) nanoarchitectures so that the capacity per area is the same for all three geometries. The low rate transport characteristics of the solid-state electrolyte means the fastest transport mechanism for Li^+ ion is through the electrode rather than the electrolyte and that little lithiation takes place at the electrode sidewall. This means the increase in electrode height required for the nanoarchitectures does not create shorter Li^+ ion transport distances when used with a solid state electrolyte and lithiation is concentrated at the tip of the electrode while the increase in electrode thickness negatively impacts the performance of the battery as the electrons produced from lithiation at the tip of the electrode have a greater distance to travel to the base of the electrode.

An improvement in the performance of the nanoarchitected batteries can be seen with an improvement in electrolyte diffusion characteristics. It can be concluded that the geometric

characteristics of the nanoarchitectures become dominant with improving electrolyte lithium ion transport. Interestingly this can be seen to have its own problems for the 3D nanoarchitecture where the lithium transport in the liquid electrolyte is fast, causing high lithium ion insertion at the base of the electrode, closest the current collector, resulting in non-uniform utilisation of the 3D nanoarchitecture. The lithium transport in the polymer-gel electrolyte is slower but results in more uniform utilisation of the electrode material due to simultaneous lithium ion insertion at the base of the 3D nanoarchitecture and at the tip due to the slower transport properties of the polymer-gel making lithium ion insertion more favourable at increased distances from the current collector. This is in agreement with Zadin et al. who found that polymer electrolytes gave more uniform electrochemical activity than liquid electrolytes in 3D interdigitated for micron scale electrode materials [9].

The 3D core-shell nanoarchitecture does not have the same problems as the 3D nanoarchitectures with improving electrolyte characteristics. The core current collector ensures that lithium insertion is uniform because of the increase in electrode/current collector area resulting in shorter distance from the current collector to the electrode/electrolyte interface. This means that the 3D core-shell nanoarchitecture maximise the advantageous effect of increased surface area when lithium ion transport in the electrolyte is the dominant transport mechanism in the cell.

The simulations suggest the implementation of nanoarchitectures such as 3D and 3D core-shell nanoarchitectures when coupled with the appropriate electrolytes can have a significant advantage in terms of areal energy and power capabilities compared to a thin-film geometry for a microbattery cell. The deployment of these architectures for microbatteries where area is at a premium and high power capabilities are desirable should result in better performing hybrid systems and less complex power management systems.

Acknowledgments

The authors would like to acknowledge the financial support from Science Foundation Ireland (SFI) Grant number: 12/IP/1722, Nanomaterials design and fabrication for energy storage. This work is supported in part by a research grant from SFI co-funded by the European Regional Development Fund under Grant Number 13/RC/2077.

References

- [1] P.V. Kamat, *J. Phys. Chem. C*, 112 (2008) 18737-18753.
- [2] B.J. Neudecker, N.J. Dudney, J.B. Bates, *J. Electrochem. Soc.*, 147 (2000) 517-523.
- [3] T. Chowdhury, D.P. Casey, J.F. Rohan, *Electrochem. Commun.*, 11 (2009) 1203-1206.
- [4] G.W. Rubloff, S.B. Lee, *Curr. Opin. Solid State Mater. Sci.*, 19 (2015) 227-234.
- [5] J.F. Rohan, M. Hasan, S. Patil, D.P. Casey, T. Clancy, *Energy Storage: Battery Materials and Architectures at the Nanoscale*, in: *ICT - Energy - Concepts Towards Zero - Power Information and Communication Technology*, 2014.
- [6] J.F.M. Oudenhoven, L. Baggetto, P.H.L. Notten, *Advanced Energy Materials*, 1 (2011) 10-33.
- [7] R.W. Hart, H.S. White, B. Dunn, D.R. Rolison, *Electrochem. Commun.*, 5 (2003) 120-123.
- [8] V. Zadin, H. Kasemagi, A. Aabloo, D. Brandell, *J. Power Sources*, 195 (2010) 6218-6224.
- [9] V. Zadin, D. Brandell, *Electrochim. Acta*, 57 (2011) 237-243.
- [10] V. Zadin, D. Brandell, H. Kasemagi, A. Aabloo, J.O. Thomas, *Solid State Ionics*, 192 (2011) 279-283.
- [11] P. Priimägi, D. Brandell, S. Srivastav, A. Aabloo, H. Kasemagi, V. Zadin, *Electrochim. Acta*, 209 (2016) 138-148.
- [12] D. Miranda, C.M. Costa, A.M. Almeida, S. Lanceros-Méndez, *Applied Energy*, 165 (2016) 318-328.
- [13] M. Doyle, T.F. Fuller, J. Newman, *J. Electrochem. Soc.*, 140 (1993) 1526-1533.
- [14] J. Newman, K.E. Thomas, H. Hafezi, D.R. Wheeler, *J. Power Sources*, 119 (2003) 838-843.
- [15] D. Danilov, R.A.H. Niessen, P.H.L. Notten, *J. Electrochem. Soc.*, 158 (2011) A215-A222.
- [16] T.M. Clancy, J.F. Rohan, *ChemElectroChem*, 5 (2018) 3273-3278.
- [17] A. Bates, S. Mukherjee, N. Schuppert, B. Son, J.G. Kim, S. Park, *International Journal of Energy Research*, 39 (2015) 1505-1518.
- [18] M.S. Whittingham, *Chem. Rev.*, 104 (2004) 4271-4302.

- [19] Y. Matsuda, N. Kuwata, J. Kawamura, *Solid State Ionics*, 320 (2018) 38-44.
- [20] G.K. Creffield, M.G. Down, R.J. Pulham, *J. Chem. Soc., Dalton Trans.*, (1974) 2325-2329.
- [21] M. Marcinek, J. Syzdek, M. Marczewski, M. Piszcz, L. Niedzicki, M. Kalita, A. Plewa-Marczewska, A. Bitner, P. Wieczorek, T. Trzeciak, M. Kasprzyk, P. Łęzak, Z. Zukowska, A. Zalewska, W. Wieczorek, *Solid State Ionics*, 276 (2015) 107-126.
- [22] Y.R. Su, J.C. Falgenhauer, C. Lupo, B.K. Meyer, D. Schlettwein, A. Polity, J. Janek, *Meeting Abstracts, MA2015-01* (2015) 103.
- [23] L. Long, S. Wang, M. Xiao, Y. Meng, *J. Mater. Chem. A*, 4 (2016) 10038-10069.